A Simulation Study of BrachyShade, a Shadow-Based Internal Source Tracking System for HDR Prostate Brachytherapy

Roumani Alabd[1], Mitra Safavi-Naeini[2], Keenan J. Wilson[1], Anatoly B. Rosenfeld[3] and Daniel R. Franklin[1]

[1] School of Electrical and Data Engineering, University of Technology Sydney, Ultimo NSW 2007, Australia

[2] Australian Nuclear Science and Technology Organisation, Lucas Heights NSW 2234, Australia

[3] Centre for Medical Radiation Physics, University of Wollongong, Wollongong NSW 2522, Australia

E-mail: `Daniel.Franklin@uts.edu.au`

E-mail: `anatoly@uow.edu.au`

Abstract. This paper presents a simulation study of BrachyShade, a proposed internal source-tracking system for real time quality assurance in high dose rate prostate brachytherapy. BrachyShade consists of a set of spherical tungsten occluders located above a pixellated silicon photodetector. The source location is estimated by minimising the mean squared error between a parametric model of the shadow image and acquired images of the shadows projected on the detector plane. A novel algorithm is finally employed to correct the systemic error resulting from Compton scattering in the medium. The worst-case error obtained with BrachyShade for a 13.5 ms image acquisition is less than 1.3 mm in the most distant part of the treatment volume, while for 75% of source locations an error of less than 0.42 mm was achieved.

Submitted to: *Phys. Med. Biol.*

1. Introduction

Prostate cancer is the second most commonly diagnosed cancer (after non-melanoma skin cancer) and one of the leading causes of cancer death among males in Australia and worldwide (Gambarini et al., 2014). In 2017, it is estimated that there will be 16,665 new cases of prostate cancer and 3,452 deaths in Australia; in the United States, the respective figures are 161,360 and 26,730 (AIHW National Mortality Database, 2017; Siegel et al., 2015; The American Cancer Society, 2017; Cancer Research UK, 2017).

High dose rate (HDR) brachytherapy is a popular form of radiotherapy commonly used for treating prostate cancer. In HDR prostate brachytherapy (HDR PBT), a small sealed capsule containing a high-activity radioactive source (typically ^{192}Ir or ^{60}Co) is temporarily placed inside or adjacent to the target area. A robotic afterloader automatically steps the radioactive source through a planned sequence of positions in an array of catheters pre-implanted in the target area by the treating physician, progressively delivering the specified radiation dose distribution throughout the target volume. The accuracy of source placement is critical to the success of HDR brachytherapy treatment, where the objective is to conformally deliver the prescribed radiation dose to the target volume while limiting the incidental dose delivered to surrounding radiation-sensitive healthy organs and tissues.

Deviations between the planned source positions and the actual positions achieved during treatment can occur due to anatomical changes (e.g. due to intra-treatment swelling or involuntary bowel or bladder movement), afterloader error or imperfect catheter placement Kirisits et al., 2014. These deviations will result in a discrepency between the planned and actual dose delivered to the target volume, potentially harming healthy tissue or under-irradiating diseased tissue. Therefore, a reliable, accurate, real-time 3D source tracking capability would be valuable for treatment quality assurance; it could also potentially adjust a treatment plan in real-time if positioning discrepancies are detected.

Several previous systems have been developed for source tracking during HDR prostate brachytherapy, as detailed in Section 2; of these, one of the most promising source tracking scheme currently available with true real-time 3D source tracking capabilities is HDR BrachyView, developed by the University of Wollongong's Centre for Medical Radiation Physics. This device is essentially an in-body pinhole camera with an integrated trans-rectal ultrasound (TRUS) probe. The camera combines a multi-double-cone pinhole tungsten collimator with a high-resolution pixelated silicon photodetector array, and the projected images of the source are analysed to estimate the source position. While this device effectively solves the problem of real-time source tracking for HDR prostate brachytherapy, the collimator is challenging to manufacture, and the device must be rotated in situ in order to cover the entire volume.

This paper proposes a source tracking system, *HDR BrachyShade*, which is inspired by HDR BrachyView, but takes a very different approach to source tracking. The key idea is to use shadows of spherical tungsten occluders rather than projections through pinholes in a tungsten collimator as the means of determining the source position. This approach offers several advantages over the original design. Firstly, high-precision spherical tungsten or tungsten alloy ball bearings are a low-cost commodity item already in widespread industrial use, and the remainder of the probe may be fabricated from any medical-grade polymer - or even 3D printed - with great precision. This avoids the problem of accurately machining off-centre

holes in a hard tungsten cylinder, which is necessary in HDR BrachyView due to the unavoidable asymmetry of the detector's printed circuit board (PCB). Secondly, a higher photon flux reaches the detector surface compared to the original BrachyView design; therefore, high-quality images may be acquired at a higher frame rate. Thirdly, unlike a double-cone pinhole in a cylindrical-shell collimator, a spherical occluder is entirely orientation-agnostic; it presents the same view to the source regardless of its relative orientation. This makes the derivation of a good analytic approximation of the relation between source position, occluder location and detected image quite straightforward. Using this analytic model, the source position may be estimated using an iterative error-minimisation algorithm, together with an empirical model of the effects of Compton scattering within the medium. Finally, the orientation-agnosticism of the spherical occluders mean that additional occluders may be placed on either side of the central axis. This greatly expands the field of view of the detector, allowing the entire prostate volume to be monitored without the need to mechanically rotate the probe. Simulation studies have confirmed the properties of the proposed design and source tracking methodology; the probe's accuracy compares favourably to the results previously published for HDR BrachyView. The probe is designed to be able to determine the source location with an accuracy of better than 0.5 mm for any point within a $40 \times 40 \times 40$ mm cubic volume, with its centre located 40 mm above the centre of the detector; this is equivalent to the volume which can be imaged by HDR BrachyView.

Section 2 presents a summary of current techniques and devices used for source tracking or dosimetry validation in HDR brachytherapy. Section 3 describes the design of the probe, and the position estimation and Compton scatter correction algorithms, and describes the simulations conducted to evaluate the accuracy of the source tracking method. Section 4 presents the results of this simulation study, including an evaluation of the efficacy of the Compton scatter correction method. Section 5 discusses the implications of the results and compares the results to experimental results published for HDR BrachyView. Finally, Section 6 concludes the paper and discusses the next steps in the development of this design, including the first planned prototype and plans for preclinical evaluation.

2. Related Work

Several dosimetric and imaging systems have been proposed to obtain an estimate of the delivered dose distribution or to verify the source position during HDR prostate brachytherapy. Although thermoluminescent dosimeters (TLDs) have been used extensively to verify the absorbed dose at a given location of interest, these passive dosimetry systems are incapable of providing measurements in real-time (Figueroa et al., 2008; Batic et al., 2011; Lambert et al., 2007). An alternative approach is to use an external solid-state semiconductor radiation detector system to monitor the source position for quality assurance (QA) in HDR PBT. Since the dose rate from an isotropic radiation source is inversely proportional to the square of the distance to the detector, this may result in either a significant uncertainty in the estimation of the source location or an acquisition time exceeding that needed for real time source tracking (Han, 2015; Lambert et al., 2007).

More accurate measurements can be made if a compact radiation sensing system is placed internally in the patient in close proximity to the treatment volume. Several different methods have been proposed for in-body real-time HDR brachytherapy QA

using various detector or dosimetry systems, including MOSFETs, diodes and plastic scintillation detectors. While these systems can provide a good estimate of the delivered dose and/or source position, most are either incapable of providing *real-time* tracking information, are difficult to place comfortably inside the body, or are unable to provide a sufficiently accurate estimate of source position (although they may offer accurate dosimetry capabilities) (Reniers et al., 2012). For example, Lambert et al. (2007) reported that although diamond detectors have been shown to offer adequate sensitivity for HDR-PT QA with good radiation resistance, they are impractically bulky, rendering them unsuitable for in-body applications. The diamond detector also exhibited significant dose rate dependence and non-linearity at higher dose rates (Therriault-Proulx et al., 2011).

Real-time dosimetry systems based on diode detectors have been used for dose verification in HDR brachytherapy treatment. Although these systems can provide rapid processing time and robust accuracy, their sensitivity is highly dependent on distance to the source (Gambarini et al., 2014; Qi et al., 2012; Therriault-Proulx et al., 2011). Seymour et al. (2011) investigated the use of a dosimeter consisting of an array of five PTW diodes for estimating the dose delivered by a HDR-PBT source inside the rectum. Dose values for 28 patients were acquired, and the deviations between the device measurement and planned dose in 71% of the measured points were ±10%. However, the error increased to ±20% when the fraction of points measured increased from 71.1% to 95%. The results have shown that this system is only suitable for select patients as the system is not always capable of being applied for subsequent fractions; it is also only able to provide measurements for gross error in the delivered dose rather than determining the distribution of that error. A further shortcoming of this approach is that the diodes' sensitivity decreases as the angle between the source and the diode array increases, which can significantly degrade the accuracy of the results.

Multi-point MOSFET detectors have been investigated for real-time dose measurements during HDR PBT. These devices are very compact, offer good spatial resolution and can provide immediate dose readout, making them a promising candidate for QA in HDR-PBT (Gambarini et al., 2012; Gambarini et al., 2014; Lambert et al., 2007; Qi et al., 2012). However, the law and variation in sensitivity of the recorded dose, the non-water equivalence of the detector and the angular dependence of MOSFET detectors limit the use of this system for accurate in-body brachytherapy dosimetry (Lambert et al., 2007; Therriault-Proulx et al., 2011; Wootton et al., 2014). A study using micro-MOSFETs for in-body dosimetry was performed by Qi et al. (2012) to evaluate the dose received by a patient undergoing HDR intracavitary brachytherapy of nasopharyngeal carcinoma (NPC). They investigated the use of an array of five MOSFETs which were calibrated independently in a water phantom, resulting in dose calibration factor of 0.46 ± 0.012 Gy/mV for the ^{192}Ir source. Dose values for 11 NPC patients were obtained with a good agreement with the predicted dose measurements of -0.3 ± 3.9% (right side) and -0.3 ± 3.7% (left side).

A recent dosimetric study conducted by Gambarini et al. (2014) used MOSkin detectors to perform real-time *in-vivo* dose measurements during prostate brachytherapy. They conducted their experiments inside a urethral catheter in a gel phantom (emulating a real prostate) and using an ^{192}Ir radioactive source with an active length of 3.6 mm. Single and dual-MOSkin detectors were calibrated in a water phantom at a distance of 38 mm from the source. The maximum discrepancy between

the planned and measured dose was 8.9% and 3.8% for single and dual MOSkin detectors respectively.

Plastic scintillation detectors (PSDs) have been proposed as a mechanism for real-time verification of HDR brachytherapy treatment. Plastic scintillation detectors are compact and water-equivalent, while providing good dose linearity, independence to dose rate, fast response, temperature independence and energy independence above 100 KeV, and as such are an attractive candidate for in-body dosimetry and imaging (Cartwright et al., 2010; Therriault-Proulx et al., 2013; Wootton et al., 2014). A clinical study conducted with an in-body plastic scintilltor detector system was performed by Therriault-Proulx et al. (2011) to determine the feasibility of using PSDs for QA during ^{192}Ir HDR prostate brachytherapy treatment. The proposed system consists of a green plastic scintillator fibre, 1 mm in diameter and 3 mm long, coupled to a light-shielded 1 mm × 7 mm optical fibre. A total of 13 parallel catheters were inserted in a water phantom (35 cm × 35 cm × 25 cm), and the ratio of the measured dose in 43 specific dwell positions with dwell time of 5 s compared to the dose predicted by the treatment planing system (TPS). The dosimetry system recorded a delivered dose of 99.6 ± 3.2% to 100.5 ± 1.5% and 104.3 ± 0.3% of the planned dose in the urethra and the rectal wall, respectively.

A second design based on PSDs, known as *Brachy*FOD, was described by Cartwright et al. (2010), in which an insertable applicator was developed for in-body use which provides real-time dose mapping and source tracking of an HDR prostate brachytherapy source. In this study, the deviation between the planned and measured dose was found to range from 2% to 3%, and the average error between the predicted and the calculated source position was approximately 2 mm. However, the authors noted that the error in estimating the source position can be up to 9 mm when the distance between the source and the scintillator is more than 100 mm.

Duan et al. (2001) investigated the use of a pinhole-based imaging system for in-body monitoring and verification of ^{192}Ir HDR brachytherapy. The developed system consists of a pinhole collimator combined with an X-ray fluoroscope and a radiographic film-screen. This system can recognise source images for dwell times ranging from 2 to 400 s with an error between the planned and reconstructed dwell positions varying from 0.3 to 0.8 mm. However, the authors discussed the limitations of their technique and indicated that their method is not applicable in clinical cases of short dwell times due to the limited dynamic range of the screen-film combinations. It is also not able to provide real-time source tracking capabilities as the film image cannot be accessed until after the procedure.

Smith et al. (2013) developed a source-tracking and dosimetry system which estimates the 3D position of an HDR brachytherapy source by fitting a Lorentz (Cauchy) function to intensity profiles of the 2D radiation distribution projected onto a large external electronic portal imaging device (EPID) - a copper build-up layer and scintillating screen coupled to an array of amorphous silicon photodiodes. The uncertainty in position estimation is dominated by the z-component, which is up to 2 mm for the greatest source-detector distance. To achieve this accuracy, an acquisition time of 10 seconds was required. The long acquisition time required to achieve this sensitivity is due to the large source-detector distance necessary for this type of source tracking system; much of the available information in the image is also discarded, since only profiles through the point of maximum intensity are fitted.

The verification of catheter position in HDR prostate brachytherapy via electromagnetic tracking has been proposed by several authors, including Poulin et al.

(2015) and Beaulieu et al. (2018), as an alternative to CT verification of catheter position post-implantation/pre-irradiation. The EM tracking system evaluated by Beaulieu et al. (2018) was shown to outperform clinical CT, with a worst-case error of 1.25 mm for tip tracking and 1.91 mm for the overall catheter position for acquisitions of 10 seconds per catheter. However, to date most research with such electromagnetic tracking systems has concentrated on verifying catheter posititition prior to irradiation rather than tracking the source itself; post-implantation tissue swelling, involuntary patient movement and other factors may introduce further deviations from the planned source position by the start of the first or subsequent fractions.

2.1. HDR BrachyView

One of the most promising innovations for HDR PBT QA is the BrachyView family of devices, developed at the University of Wollongong's Centre for Medical Radiation Physics, with two separate variants proposed for HDR and LDR PBT by Safavi-Naeini et al. (2013) and Petasecca et al. (2013) and Alnaghy et al. (2017), respectively. HDR BrachyView performs real-time monitoring of the position of the ^{192}Ir source during HDR prostate brachytherapy treatment. The probe consists of a semi-cylindrical tungsten pinhole collimator, suspended 6.5 mm over a 4×1 array of *Timepix* pixellated silicon detectors. Source tracking is performed by locating the centres of mass of each projection of the source on the imaging plane, back-projecting lines through the pinholes, and identifying the point of maximum convergence. The probe's performance has been evaluated both via Monte Carlo simulation and experiment, with the maximum overall error between the planned and measured source position being 1 mm for the majority of evaluated source positions located in the target volume (a 40 mm × 40 mm × 40 mm volume above the detector). However, the error in estimated source position increases when the distance between the detector and the source is larger, reaching a maximum of 1.3 mm for a source which lies in the extreme corners of the treatment volume. Sensitivity also varies depending on the arrival angle of the photons at the pinholes, restricting its field of view (FoV) to the acceptance angle of the double-cone pinholes; therefore, to monitor the entire potential treatment volume, it may be necessary to mechanically rotate the probe in situ, depending on whether the source will move beyond the detector FoV for a single angular orientation of the probe. Finally, due to the fact that most incident photons are blocked by the collimator, overall detector sensitivity is limited by the size of the pinholes (as there is an intrinsic trade-off between sensitivity and pinhole camera resolution (Alnaghy et al., 2016). The minimum acquisition time needed to obtain images of sufficient quality for sub-millimetre tracking accuracy is around 300 ms.

In summary, one of the most promising systems for real-time HDR prostate brachytherapy QA is HDR BrachyView; however, there remains an opportunity for further improvement in ease of manufacturing, acquisition speed and FoV coverage.
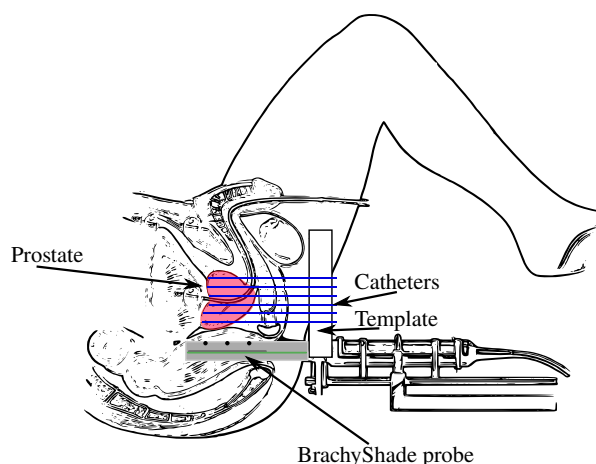
3. Materials and Methods

3.1. Probe Design

The probe consists of a linear 4×1 array of silicon Timepix detectors, positioned in the centre of a cylindrical plastic shell with an outer diameter of 24 mm. The shell has a thickness of 4 mm, with a 1.5 mm groove cut in both inner surfaces, to support
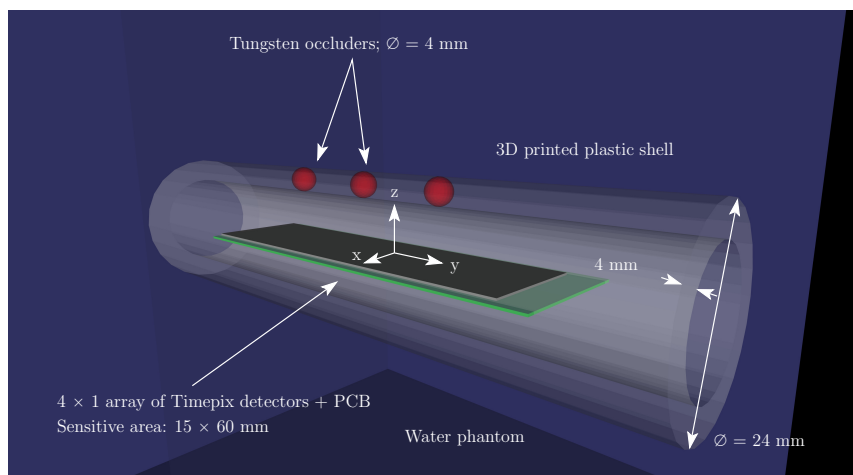
Figure 1. The BrachyShade probe.

.

Figure 2. Clinical context of BrachyShade.

.

the printed circuit board (PCB) on which the Timepix detectors are mounted. Three spheres of MT-18F tungsten alloy (95% W, 3.5% Ni, 1.5% Fe), 4 mm in diameter, are embedded in the plastic shell, with their centres located 10 mm above the centre of the detector plane, directly above the midpoints of the joints between adjacent Timepix detectors. The FoV of the detector is defined as the wedge-shaped volume above the detector in which the source will project a partial shadow onto the detector plane. A 3D rendering of the proposed design is shown in Figure1; the use of the probe, showing its location relative to the prostate, is shown in Figure 2.

The geometry of the probe, including the number and location of occluders, has been chosen to maximise the FoV. The occluders may be positioned closer to the detector to increase the FoV; however, this is at the cost of reduced spatial resolution in the estimated source position. The field of view limitation does not seriously impede

the function of the imaging system; for cases where the FoV is insufficient to capture all movements of the source, the probe may be sheathed in a thin plastic shell which remains fixed while allowing the probe to rotate; alternatively, additional occluder configurations (for example, two pairs of occluders placed on either side of the central axis of the probe at a 45° angular offset from the vertical) can be used to increase the FoV.

Each Timepix detector itself consists of a square silicon slab, 300 μm thick and 14 mm across, divided into a 256×256 array of square pixels with a pitch of 55 μm. Readout from an array of Timepix detectors can be performed using an interface such as FITpix, which enables data acquisition via a USB2.0 port on a host PC. A FITpix interface coupled to a single Timepix detector can theoretically read out up to 90 frames per second, with a dead time of 11 ms between frames during which no charge can be collected; in practice, acquisition times of 100 ms or more are typically used. The Timepix detector can operate in several different modes: it can collect per-pixel particle/photon counts, per-pixel spectroscopic data or per-pixel time of arrival data. For this project, the Timepix is operated in count mode.

Coregistration of the probe (and hence the estimated source position) with the prostate is achieved via TRUS. The external rigid plastic shell remains in place, the BrachyShade probe is withdrawn and a modified TRUS probe is inserted, acoustically coupled to the external shell via ultrasound gel. This procedure may be repeated several times during the procedure to monitor the position of the prostate relative to the coordinate system of the probe, to account for peristaltic and other involuntary patient motion. This is similar to the procedures used with BrachyView probes, as described in Alnaghy et al. (2017).

3.2. Source Position Estimation Algorithm

The source position estimation algorithm is based on an analytic model of the expected pattern of photons which interact with the detector plane, given the source and occluder positions, which is described in detail in Section 3.3. From a starting point somewhere in the volume above the occluders, the analytic model is used to generate the expected detected photon distribution on the detector. The mean squared error between the detected photon map and the image acquired by the Timepix array is then iteratively minimised by adjusting the estimated source position using the Levenberg-Marquardt algorithm, until the algorithm converges or an arbitrary maximum number of iterations is reached. Convergence is normally achieved in less than 30 iterations; the hard limit is set to 100.

In reality, however, the analytic model is imperfect; specifically it does not account for the effects of Compton scatter in the medium. However, the effects of Compton scatter on the estimated source position are quite deterministic, and can be corrected using a simple empirically-derived error model, described in detail in Section 3.4.

3.3. Analytic Model

The model uses a right-handed coordinate system with its origin located at the physical centre of the sensitive volume of the detector array, as shown in Figure 3. The source is assumed to be an ^{192}Ir point source located at position $P_s = (x_s, y_s, z_s)$; the occluders are placed at $O_k = (0, y_{o,k}, z_o)$ mm, $k \in [1, 2, 3]$. Photons emitted from this source are subject to a number of possible sources of attenuation and Compton scattering.
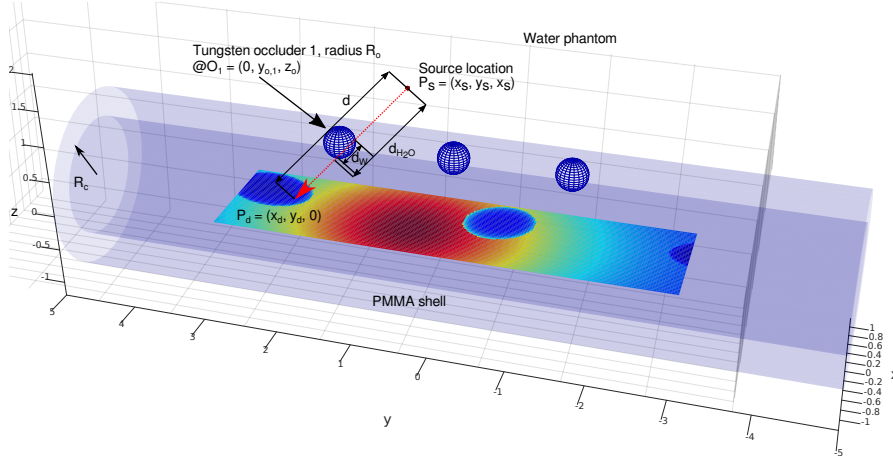
Figure 3. Analytic model, showing all key geometric parameters. The source is located at $P_s = (2.5, 5.0, 20)$ mm.

Firstly, the photon path intersects with a volume of water (or approximately water-equivalent tissue). Secondly, it may traverse a maximum of one tungsten-alloy sphere (it is possible for the photon path to intersect with more than one sphere only if the source is located outside of the prostate volume). Finally, any detectable photon will pass through the plastic shell (which is approximately tissue-equivalent) and a small volume of air in the void above the detector, before reaching the detector plane. Photons arriving at the detector may or may not be detected, with the probability of detection dependent on the energy of the photon and the angle of arrival. The Timepix is operated in count mode, with a conservative energy threshold of 16 keV.

To estimate the distribution of photons which would be detected for a given source location, a map of the gamma photon intensity which would arrive at the detector in the absence of media between the source and the detector is generated. At a distance d from a source emitting N photons of a particular wavelength per unit time, the flux density $\phi(d)$ at distance d in units of photons per unit time per unit area will be given by:

$$\phi(d) = \frac{N}{4\pi d^2}$$

At a point $P_d = (x_d, y_d, 0)$ on the detector plane, $d = \sqrt{(x_d - x_s)^2 + (y_d - y_s)^2 + z_s^2}$. Furthermore, the angle between the normal of an infinitesimal area dA centred at $(x_d, y_d, 0)$ on the detector plane to the line joining it to the source position is given by $\sin^{-1}\left(z_s / \sqrt{(x_d - x_s)^2 + (y_d - y_s)^2 + z_s^2}\right)$; therefore, the flux density at the surface, based on free-space path loss only, will be:

$$\phi_{fs}(x_d, y_d) = \frac{N}{4\pi((x_d - x_s)^2 + (y_d - y_s)^2 + z_s^2)}$$
$$\times \frac{z_s}{\sqrt{(x_d - x_s)^2 + (y_d - y_s)^2 + z_s^2}}$$
$$= \frac{N z_s}{4\pi((x_d - x_s)^2 + (y_d - y_s)^2 + z_s^2)^{\frac{3}{2}}}$$

The path length through water can be calculated by finding the distance from the source to the point of intersection between the line from P_d to P_s and the inner surface of the cylinder. The cylinder itself is assumed to be water-equivalent. We assume that water only attenuates incident gamma photons and do not attempt to model Compton scattering. This assumption is not valid in practice; however, analytic modelling of Compton scatter is difficult and computationally expensive, since in order to determine the effect of scatter on the shadows, the angle of arrival would need to be computed for each photon, negating the value of an analytic model. Instead, we ignore scattering at this stage and apply an empirical correction factor at a later stage of the process of determining source location.

The equation of the line joining P_d and P_s is:

$$\begin{bmatrix} x \\ y \\ z \end{bmatrix} = \begin{bmatrix} x_d \\ y_d \\ 0 \end{bmatrix} + t \begin{bmatrix} l_x \\ l_y \\ l_z \end{bmatrix} \tag{1}$$

where t is the distance along this line from P_d, $l_x = (x_s - x_d)/d$, $l_y = (y_s - y_d)/d$, $l_z = z_s/d$ and $d = \sqrt{(x_s - x_d)^2 + (y_s - y_d)^2 + z_s^2}$. Solving for the point of intersection between this line and the inner surface of the cylinder (with radius R_c) reduces to finding the point of intersection between the upper half of a circle of radius R_c and the projection of the previously-mentioned line on the xz plane, since the cylinder is parallel to the y axis:

$$R_c^2 = (x_d + tl_x)^2 + (tl_z)^2$$

Re-arranging to solve for parameter t (for the positive semicircle only, i.e. the upper half-cylinder):

$$t = -\frac{x_d l_x + \sqrt{x_d^2 l_x^2 - (l_x^2 + l_z^2)(x_d^2 - R_c^2)}}{l_x^2 + l_z^2}$$

This parameter can be substituted back into (1) to solve for the coordinates of the point of intersection, which allows the distance through water by a photon emitted by the source arriving at the detector plane to be calculated, and hence the probability that this photon will be absorbed or transmitted through that space:

$$\begin{aligned} p_x &= x_d + tl_x \\ p_y &= y_d + tl_y \\ p_z &= z_d l_z \\ d_{H_2O} &= \sqrt{(p_x - x_s)^2 + (p_y - y_s)^2 + (p_z - z_s)^2} \end{aligned} \tag{2}$$

For each of the k tungsten-alloy occluders, (1) can be solved simultaneously with the equation of a sphere of radius R_o centred at O_k. This results in a quadratic equation, with the discriminant:

$$\begin{aligned} \Delta &= ((x_s - x_d)x_d + (y_s - y_d)(y_d - y_s) - z_s z_o)^2 \\ &\quad - (x_d^2 + (y_d - y_s)^2 + z_o^2) + R_o^2 \end{aligned} \tag{3}$$

If this discriminant is positive, the line from the detector plane to the source intersects with the tungsten-alloy sphere. Therefore, the total path length through the occluder is:

$$d_W = \begin{cases} 2\sqrt{\Delta} & \Delta > 0 \\ 0 & \Delta \leq 0 \end{cases}$$

The path length through the occluder, if any, is also subtracted from the path length through water. The number of photons of wavelength λ_i per unit time per unit area arriving at the surface of the detector are then:

$$\phi_{arr}(x_d, y_d) = \phi_{fs}(x_d, y_d)e^{-\mu_{H_2O}(\lambda_i)(d_{H_2O}-d_W)}e^{-\mu_W(\lambda_i)d_W}$$

where $\mu_{H_2O}(\lambda_i)$ and $\mu_W(\lambda_i)$ are the linear attenuation coefficients of water and tungsten alloy at wavelength λ_i, respectively. The number of photons which deposit some energy during their interaction with the detector (either photoelectrically or, more frequently, through Compton scattering) per unit time per unit area depends on the thickness of silicon through which they pass, which in turn depends on the angle of arrival - a simple function of the relative position of the source and the point on the detector and the thickness of the detector, t_{det}. To simplify the analytic model, we ignore the fact that the path from the source to a given pixel on the detector may intersect with more than one pixel, and assign the totality of interaction probability to the pixel centred at (x_d, y_d):

$$\phi_{det}(x_d, y_d) \approx \phi_{arr}\left(1 - e^{-\frac{d}{z_s}t_{det}\mu_{Si}(\lambda_i)}\right)$$

To generate a good approximation of the expected map of detected photons for a given source position (x_S, y_s, z_s), the area of the detector is quantised into individual pixels (in the case of the Timepix detector, these pixels are each 55 μm × 55 μm in size), ϕ_{det} is calculated at the centre of each pixel for each wavelength present in the source spectrum, multiplied by the area of the pixel and the duration of the observation; the total count is summed by weights corresponding to the relative distribution of wavelengths in the source spectrum.

3.4. Compton Scatter Correction

While the analytic model described in Section 3.3 provides a good estimate of the shadow map in the absence of a scattering medium, the probe is intended for use inside the human body, where Compton scattering is significant. Compton scattering reduces the contrast between the illuminated and shadowed regions, since some photons can 'go around' the occluders. The discrepancy between the physical process and the analytic model has a relatively small impact on the accuracy of the estimate of the position in the x and y dimensions; however, it results in a significant overestimate (of the order of 10%) of the source position in z. Analytic modelling of the three-dimensional distribution of photon paths from a point source in a Compton-scattering medium is complex; most published models for Compton scatter only attempt to estimate spectra or dose distribution on a plane for a point source in a uniform medium (i.e., without the presence of occluding objects).

Instead, in this work, an empirical model is used to model and correct the effects of Compton scatter on the estimated source position. Defining the volume of interest as a 40 mm × 40 mm × 40 mm cube centred at $(0, 0, 40)$ mm, it may be observed that both the BrachyShade probe itself and the volume of interest (VoI) are symmetric

about both the xz and yz planes. Therefore, a model developed for correcting the error in the positive xy quadrant of the VoI, $(0 \leq x \leq 20, 0 \leq y \leq 20, 20 \leq z \leq 50)$, can be applied to the other quadrants by symmetry. A $9 \times 9 \times 9$ equally-spaced lattice of locations is constructed within this volume, with points spaced by 2.5 mm in x and y and 5 mm in z, for a total of 729 point within the quarter-FoV. A set of Geant4 (version 10.3p2) simulations were conducted with a simulated ^{192}Ir point source placed at each of these locations. A total of 5 billion primaries were simulated; the acquired images were then used together with the fitting algorithm to estimate the source location for each point, and the error vector between the ground truth location and the estimated source positions calculated.

Two distinct classes of error vectors are observed. The first, and most useful in this work, is the set of error vectors at points for which most or all of the shadows are projected onto the detector surface, corresponding to a wedge-shaped region parallel to the y axis. In this region, denoted R_1, the error vectors point approximately towards the origin of the coordinate system, and have a magnitude of the order 10% of the distance from the origin. The magnitude and direction of this error vector vary smoothly as a function of position, implying that a relatively simple mathematical model describing the error as a function of position can be derived. The boundary of this region can easily be determined by a simple examination of the geometry of the probe - it is an inverted triangular prism with an acceptance angle of $55.3°$. A second class of points in the quarter-FoV is also observable - this is the set of points which do not project a shadow on the detector plane; these still encode some information in the detected-photon distribution, but with much less specificity, as there is little structure in the image which can be used to accurately discern source location. This region is denoted R_2. Finally, there is also a small intermediate region, R_i for which the shadow is partially on the detector plane.

Of these regions, the R_1 is of the greatest interest, since it offers the lowest error; it also corresponds to the bulk of the nominal prostate volume. R_i is also of interest, since some structure still exists in the projected image. For simplicity, the remainder of this paper assumes that the region of interest includes R_1 and the part of R_i where at least half of the shadow is visible on the imaging plane. This region is an inverted triangular prism with an acceptance angle of 73.7^circ, and its axis of translation parallel to the long axis of the probe. Like HDR BrachyView, if the FoV is insufficient to observe the entire treatment volume, it is possible to rotate the imaging system around its y axis relative to its (stationary) outer shell to achieve the desired coverage. Unlike HDR BrachyView, it is also possible to add additional lateral occluders to ensure that an orientable shadow pattern is observed even where the three primary occluders do not cast a shadow on the detector surface.

In the primary FoV region, the smoothly varying error vector field can be approximated well as a polynomial function of estimated source position. The error correction model has been implemented with a linear, second-order (quadratic) and third-order model; the quadratic model was found to result in a smaller residual error compared to the linear model, and the third-order model performs no better than the quadratic. Therefore, for the remainder of this work, a second-order quadratic model for the error field is adopted.

While it is possible to express this error field as a function of *true* source position, which makes more intuitive sense, expressing it as a function of *estimated* source position allows the error to be conveniently corrected. The problem, then, becomes one of determining the coefficients $a_{x|y|z,\{1-7\}}$ which, given the estimated position

$(\hat{x}, \hat{y}, \hat{z})$, allow the error to be determined and hence corrected:

$$
\begin{aligned}
e_x &= a_{x,1}\hat{x}^2 + a_{x,2}\hat{x} + a_{x,3}\hat{y}^2 + a_{x,4}\hat{y} + a_{x,5}\hat{z}^2 + a_{x,6}\hat{z} + a_{x,7} \\
e_y &= a_{y,1}\hat{x}^2 + a_{y,2}\hat{x} + a_{y,3}\hat{y}^2 + a_{y,4}\hat{y} + a_{y,5}\hat{z}^2 + a_{y,6}\hat{z} + a_{y,7} \\
e_z &= a_{z,1}\hat{x}^2 + a_{z,2}\hat{x} + a_{z,3}\hat{y}^2 + a_{z,4}\hat{y} + a_{z,5}\hat{z}^2 + a_{z,6}\hat{z} + a_{z,7}
\end{aligned} \tag{4}
$$

The coefficients $a_{x|y|z,\{1-7\}}$ may be calculated by constructing an system of linear equations from the estimated source positions and calculated errors within R_1, and determining the least-squares fit. An exact solution cannot be obtained, since each observation of the error is noisy (due to the statistical noise inherent in the simulation); however, the large number of points available allow a good estimate of the coefficients to be obtained.

Given a set of N non-collinear points inside the first region (with the condition that $N \gg 7$ and matrix $\mathbf{P}$, defined below, be well-conditioned), let

$$
\mathbf{E}_{x|y|z} = \begin{bmatrix}
e_{x|y|z}(1) \\
e_{x|y|z}(2) \\
e_{x|y|z}(3) \\
\dots \\
e_{x|y|z}(N)
\end{bmatrix}
$$

where $e_{x|y|z}(k)$ is the error component in x, y or z for the kth point in the first region, $k \in [1, 2, \dots, N]$. Now, defining

$$
\mathbf{P} = \begin{bmatrix}
\hat{x}(1)^2 & \hat{x}(1) & \hat{y}(1)^2 & \hat{y}(1) & \hat{z}(1)^2 & \hat{z}(1) & 1 \\
\hat{x}(2)^2 & \hat{x}(2) & \hat{y}(2)^2 & \hat{y}(2) & \hat{z}(2)^2 & \hat{z}(2) & 1 \\
\hat{x}(3)^2 & \hat{x}(3) & \hat{y}(3)^2 & \hat{y}(3) & \hat{z}(3)^2 & \hat{z}(3) & 1 \\
\dots \\
\hat{x}(N)^2 & \hat{x}(N) & \hat{y}(N)^2 & \hat{y}(N) & \hat{z}(N)^2 & \hat{z}(N) & 1
\end{bmatrix}
$$

and

$$
\mathbf{A}_{x|y|z} = \begin{bmatrix}
a_{x|y|z,1} \\
a_{x|y|z,2} \\
a_{x|y|z,3} \\
a_{x|y|z,4} \\
a_{x|y|z,5} \\
a_{x|y|z,6} \\
a_{x|y|z,7}
\end{bmatrix}
$$

(4) may be expressed in matrix form and solved by inverting $\mathbf{P}$ to determine $\mathbf{A}_{x|y|z}$:

$$
\begin{aligned}
\mathbf{E}_{x|y|z} &= \mathbf{P}\mathbf{A}_{x|y|z} \\
\mathbf{P}^{-1}\mathbf{E}_{x|y|z} &= \mathbf{P}^{-1}\mathbf{P}\mathbf{A}_{x|y|z} = \mathbf{A}_{x|y|z}
\end{aligned}
$$

Since $\mathbf{P}$ is not square (the number of rows exceeds number of columns), the Moore-Penrose pseudoinverse $\mathbf{P}^+$ is used, calculated via singular value decomposition (SVD). The resulting coefficients $\mathbf{A}_{\mathbf{x}|\mathbf{y}|\mathbf{z}}$, for the x, y and z components, respectively, represent the optimal least-squares solution to the (overdetermined) problem. These coefficients can be used, together with the estimated source location returned by the position-estimation algorithm, to provide an estimate of the error in the source location, which can simply be added to the estimated source location to provide an improved estimate $(\hat{x}', \hat{y}', \hat{z}')$ for any point inside R_1.
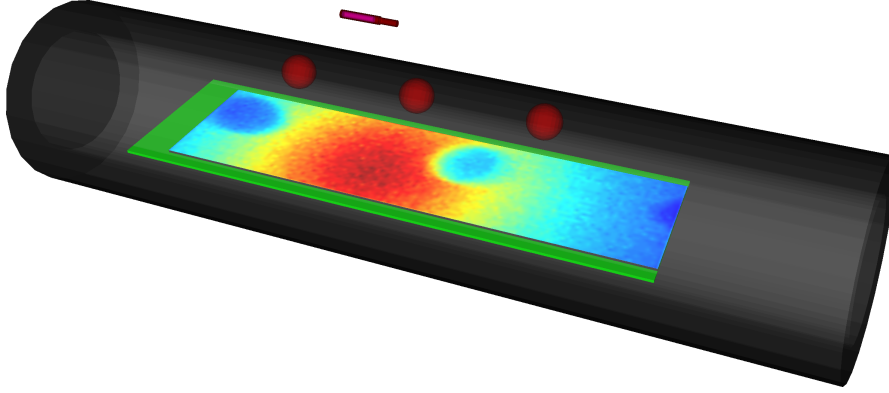
Figure 4. Simulation model in Geant4. The source is located at $P_s = (2.5, 5.0, 20)$ mm (as for Figure 3).
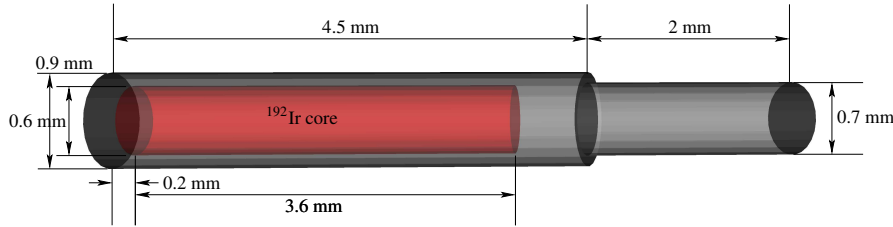
Figure 5. The simulated ^{192}Ir HDR brachytherapy source. The core consists of pure iridium with a uniform distribution of ^{192}Ir, surrounded by a steel shell (Borg et al., 1999a; Han et al., 2014).

3.5. Monte Carlo Simulations

Simulations were performed using Geant4 10.3p2. Electromagnetic interactions were modelled using the Livermore Low Energy physics package, with cuts of 1 μm in the target region and 4 mm in the phantom region, for all gamma, electron and positron interactions. For scatter correction, each of the 729 source positions was simulated with 5 billion decays. For a typical source air kerma $S_k = 4.11 \times 10^4$ μGy m^{2}h^{-1} (corresponding to an activity of 370 GBq), this corresponds to an acquisition period of 13.5 ms. True radioactive decay is not modelled; instead, photons are emitted from a uniformly distributed random location within the source model, in a uniformly distributed random direction, with the proportions of each photon energy determined according to the ^{192}Ir spectrum (see Table 1). This provides a realistic model for the spectrum of the real source, regardless of the age of the source, since ^{192}Ir decays directly into stable ^{192}Pt, with no other radioactive species produced. In the real source, all β^- radiation is blocked by the steel shell (see Figure 5).

The source model used for this work is the ^{192}Ir MicroSelectron-HDR, described by Borg et al. (1999a), Borg et al. (1999b) and Daskalov et al. (1998). The core consists of a pure iridium metal cylinder, 3.6 mm long and 0.6 mm in diameter, with ^{192}Ir uniformly distributed throughout the volume. This is surrounded by a steel shell, 4.5 mm long and 0.9 mm in diameter, which is connected to a short steel cable (2 mm long and 0.7 mm in diameter). A schematic of the source is shown in Figure 5.

Table 1. ^{192}Ir gamma spectrum (Borg et al., 1999a)

| Energy (keV)	Emitted Fraction (%)
10.5	2.45
64	4.54
75	1.22
136.5	0.0766
201.5	0.205
205.5	1.41
283.5	0.113
295.5	12.2
308.5	11.4
316.5	36.3
374.5	0.305
416.5	0.281
468.5	20.2
484.5	1.34
489.5	0.181
588.5	1.90
604.5	3.45
612.5	2.23
884.5	0.107

4. Results

4.1. Uncorrected Results

Figure 6 shows an example of simulation output and corresponding results from the fitting process. A significant and systemic error is evident; each component of the source position is overestimated, with the biggest error being in the z dimension. Upon comparison of Figures 6(a) and 6(b), it may be seen that the contrast between the shadow region and the directly illuminated part of the detector is much less in the simulation compared to the analytic model, because the analytic model does not account for Compton scattering. This results in some radiation being scattered around the occluder, illuminating parts of the detector which would be in shadow if it were not for the scattered photons. The total illumination of the detector is therefore less than the analytic model would predict for the same source position, resulting in an overall bias towards a more distant estimated source position.

4.2. Compton Scatter Correction

Figure 7(a) shows the error at each of points in one quarter of the FoV as a vector field (error vectors are shown at the same scale as the spatial dimensions in the figure). The fitted second-error polynomial model of the error field is shown in Figure 7, evaluated at all points in this volume. Note that the model is evaluated at all 729 points in the rectangular 20 mm × 20 mm ×40 mm volume; however the model is not valid outside of the field of view.

   After subtracting the estimated error from the uncorrected source position

(a) Simulation data

(b) Analytic fit
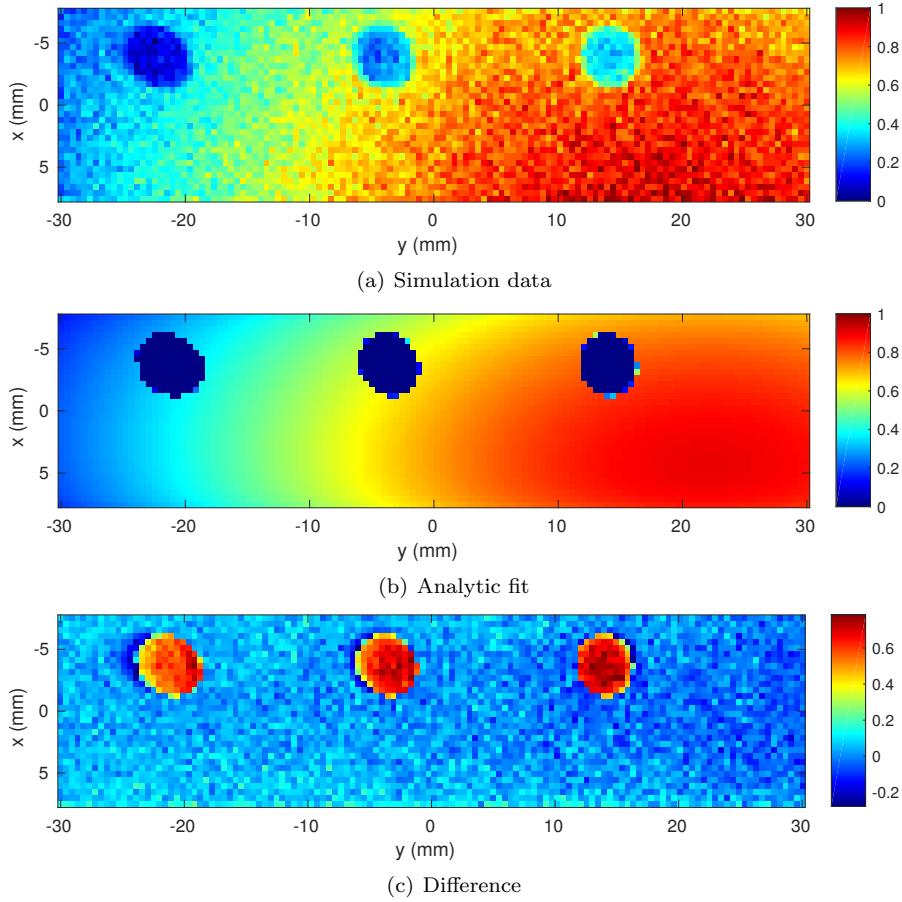
(c) Difference

Figure 6. Example of raw output from Geant4 simulations (37×10^9 primary particles, real ^{192}Ir source model centred at (18.75, 20, 60) mm), with the results of the fitting process and the difference between the two. Without Compton scatter correction, the fitting algorithm estimates the location as being (22.0, 21.9, 70.8) mm.

estimates, the residual error field is as shown in Figure 7(c).

Figure 8 shows the magnitude of the error as a function of distance from the origin, before and after Compton scatter correction. Post-correction, the error only increases slightly with increasing distance over the range of the treatment volume.

Error statistics for Compton-corrected position estimates of both point source and realistic source model simulations are shown in Table 2.

5. Discussion

For both the point source and real source model, the median error is less than 0.3 mm. In both cases, the maximum error is less than 1.5 mm (1.3 mm for the realistic source model) - however, this is an outlier (and is essentially due to the limited SNR of the 13.5 ms acquisitions of the most distant source locations). At the vast majority (more than 75%) of locations in the quarter-FoV, the post-correction error is less than

(a) Uncorrected Error Field   (b) Correction Field   (c) Corrected Error Field
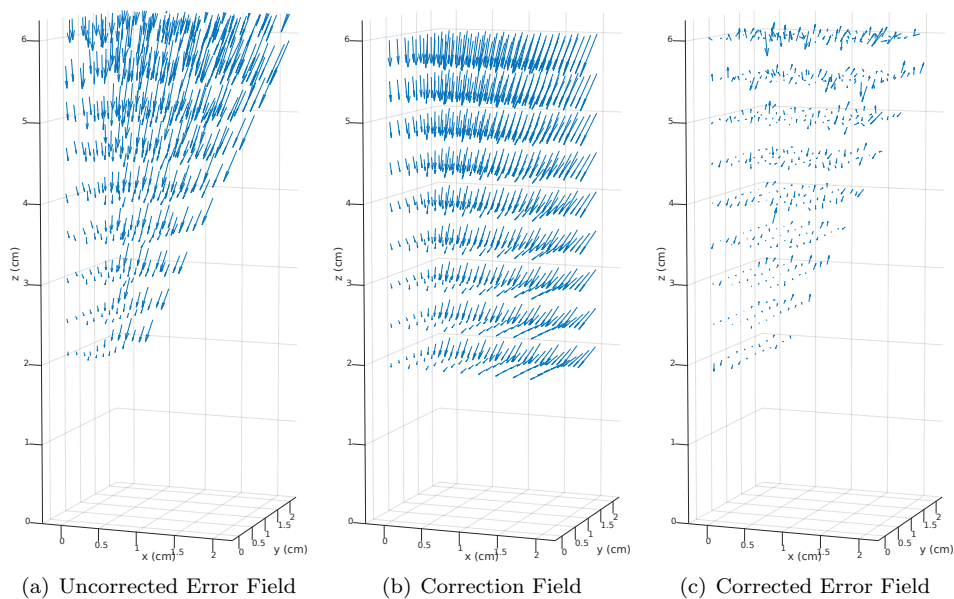
Figure 7. Error vector field as a function of estimated source position; fitted second-order polynomial model of the error vector field; residual error after correction added to original position estimate.
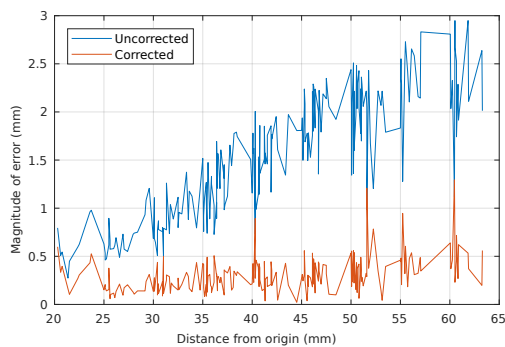
Figure 8. Error as a function of distance from (0, 0, 0), before and after applying the Compton scatter correction field.

Table 2. Magnitude of the residual error after Compton scatter correction; with an accurate model of an HDR brachytherapy source, the residual error is less than 1.137 mm for all evaluated source positions and less than 0.4141 mm in 75% of positions.

	Point source (mm)	Real source model (mm)
Minimum	0.02256	0.0223
1st quartile	0.1550	0.1831
Median	0.2291	0.2818
3rd quartile	0.3755	0.4141
Maximum	1.426	1.2941

0.5 mm. The median error is largely determined by the SNR of the image, and will be further reduced with longer acquisitions with better SNR. The probe is intended to operate with an acquisition period of 100 ms or more, which should improve the SNR by a factor of more than 2.5. The direction of the residual error field observed in Figure 7(c) is essentially random; it is no longer biased and it gradually increases with distance from centre of the detector plane (i.e. the origin of the coordinate system).

Based on the Monte Carlo simulation results presented in the preceding section, it is clear that Compton scatter correction is absolutely essential for the proper estimation of source position. The proposed correcting Compton scatter is very effective, with the residual error in the position estimate now determined principally by the SNR which can be achieved during a given acquisition interval. With the current simulation results, and with a realistic model of the radioactive source, an error of less than 1.3 mm is achievable even for acquisitions with a much lower SNR than is achievable in practice, while the majority of locations exhibit an error less than 0.5 mm. The accuracy of location estimation is comparable to that offered by HDR BrachyView (a maximum value of 1.3 mm), however it can be achieved with a significantly shorter acquisition time (in this instance, 13.5 ms compared to a minimum of 300 ms for HDR BrachyView for an equivalent level of accuracy) and with simpler and cheaper manufacturing.

For the 3-occluder HDR BrachyShade probe, the field of view is limited by the volume above the detector for which a shadow is at least partially projected onto the imaging plane. The addition of further occluders to the left and right of the three occluders modelled in this paper is straightforward, and ensures that a shadow will be projected onto the imaging plane even for much more extreme source positions, essentially extending the field of view to the entire 40 mm × 40 mm × 40 mm volume above the probe. This requires no substantial modifications of either the source position estimation algorithm or the Compton scatter correction algorithm; it does somewhat increase the execution time for evaluation of the analytic model.

The accuracy of fitting depends on both the signal to noise (SNR) of the acquired image (which in turn depends on the acquisition time and the proximity of the source) and also the pixel dimensions. Increasing pixel dimensions both increases the SNR (as each pixel will detect a larger number of photons) and decreases the spatial resolution with which the photon distribution can be measured. The pixel pitch of Timepix is 55 μ m, which is much higher than needed for this application; therefore, it is possible to improve the SNR without degrading overall accuracy by rebinning pixels into larger groups. This has the added benefit of significantly increasing the speed of the fitting process, since it greatly reduces the number of calculations needed for error minimisation. For a realistic exposure interval of 100 ms, with a typical HDR brachytherapy source air kerma strength of $S_k = 4.11 \times 10^4$ μGy m^{2}h^{-1} (corresponding to a source activity of 370 GBq), rebinning in both x and y by a factor of either 4 or 8 resulted in the best overall performance (approximately the same in both cases). This provides a 16-fold or 64-fold reduction in the number of pixels in the image, greatly accelerating the fitting process.

A multithreaded C-based implementation of the fitting algorithm converges within approximately 250-300 ms on a fast PC (quad-core 7th-generation Intel i7), allowing a 100 ms acquisition and position estimate to be completed in under 0.5 seconds; however, acquisition of the next frame may begin immediately after the transfer of the previous frame, so with more processing power and further optimisation of the algorithm, the position could be estimated every 111 ms (or less, if slightly less

precision is acceptable). This this should be feasible on recent (2018) high-end Intel and AMD CPUs.

6. Conclusion

A source tracking system was developed which uses shadows cast by tungsten occluders to identify the position of a HDR brachytherapy source in real time. Source tracking with an accuracy of better than 1.3 mm was obtained for a 13.5 ms image acquisition period (for a typical HDR brachytherapy source) at all source locations within the FoV, with the estimated source position being within 0.5 mm in the majority of locations. The Compton scatter correction algorithm was able to largely correct errors in the estimated source position which result from scattering in the medium.

The next steps planned in the development of HDR BrachyShade over the next twelve months include a detailed simulation evaluation of a 7-occluder variant with increased FoV, performance evaluation with a ^{60}Co source, performance evaluation with simulated 100 ms acquisitions for a range of points within the treatment volume, and fabrication of a prototype (currently in development) for evaluating real-world performance with an actual brachytherapy source. An alternative position-based localisation algorithm based on a high-speed template-matching algorithm is also in development, and will be compared to the method proposed in this paper.

7. Acknowledgements

References

AIHW National Mortality Database (2017). *Cancer mortality trends and projections: 2014 to 2025.* http://www.aihw.gov.au/cancer/mortality-trends-projections/. 2017.

Alnaghy, S. et al. (2017). "BrachyView: Combining LDR seed positions with transrectal ultrasound imaging in a prostate gel phantom". In: *Phys. Med.* 34 (2017), pp. 55–64.

Alnaghy, S. et al. (2016). "Analytical Modelling and Simulation of Single and Double Cone Pinholes for Real-Time In-Body Tracking of an HDR Brachytherapy Source". In: *IEEE Trans. Nucl. Sci.* 63.3 (2016), pp. 1375–1385.

Batic, M. et al. (2011). "Verification of High Dose Rate ^{192}Ir Source Position During Brachytherapy Treatment Using Silicon Pixel Detectors". In: *IEEE Trans. Nucl. Sci.* 58.5 (2011), pp. 2250–2256.

Beaulieu, L. et al. (2018). "Real-time electromagnetic tracking–based treatment platform for high-dose-rate prostate brachytherapy: Clinical workflows and end-to-end validation". In: *Brachytherapy* 17.1 (Jan. 2018), pp. 103–110.

Borg, J. et al. (1999a). *Monte Carlo Calculations of Photon Spectra in Air from ^{192}Ir Sources.* Tech. rep. PIRS-629r. Ottawa, Ontario, K1A 0R6, Canada: Institute for National Measurement Standards National Research Council, Mar. 1999.

Borg, J. et al. (1999b). "Spectra and air-kerma strength for encapsulated ^{192}Ir sources". In: *Med. Phys.* 26.11 (1999), pp. 2441–2444.

Cancer Research UK (2017). *Prostate cancer statistics.* `http : / / www . cancerresearchuk . org / health – professional / cancer – statistics / statistics – by – cancer – type / prostate – cancer ? _ga = 2 . 216659542 . 1555524786.1494556298–2024404577.1494553660. 2017.`

Cartwright, L. et al. (2010). "Dose mapping of the rectal wall during brachytherapy with an array of scintillation dosimeters". In: *Med. Phys.* 37.5 (2010), pp. 2247–2255.

Daskalov, G. M. et al. (1998). "Monte Carlo-aided dosimetry of a new high dose-rate brachytherapy source". In: *Med. Phys.* 25.11 (1998), pp. 2200–2208.

Duan, J. et al. (2001). "Real-time monitoring and verification of in vivo high dose rate brachytherapy using a pinhole camera". In: *Med. Phys.* 28.2 (2001), pp. 167–173.

Figueroa, S. D. et al. (2008). "TLD assessment of mouse dosimetry during microCT imaging". In: *Med. Phys.* 35.9 (2008), pp. 3866–3874.

Gambarini, G et al. (2012). "Solid state TL detectors for in vivo dosimetry in brachytherapy". In: *Appl. Radiat. Isot.* 71 (2012), pp. 48–51.

Gambarini, G et al. (2014). "Online in vivo dosimetry in high dose rate prostate brchytherapy with MOSkin detectors: in phantom feasibility study". In: *Appl. Radiat. Isot.* 83 (2014), pp. 222–226.

Han, Z et al. (2014). "Radiation dose enhancement at tissue-tungsten interfaces in HDR brachytherapy". In: *Phys. Med. Biol.* 59.21 (2014), p. 6659.

Han, Z. (2015). "Real-time source tacking for quality assurance in HDR prostate brachytherapy". PhD thesis. Faculty of Engineering and Information Sciences, 2015.

Kirisits, C. et al. (2014). "Review of clinical brachytherapy uncertainties: Analysis guidelines of GEC-ESTRO and the AAPM". In: *Radiother. Oncol.* 110.1 (Jan. 2014), pp. 199–212.

Lambert, J. et al. (2007). "In vivo dosimeters for HDR brachytherapy: A comparison of a diamond detector, MOSFET, TLD, and scintillation detector". In: *Med. Phys.* 34.5 (2007), pp. 1759–1765.

Petasecca, M et al. (2013). "BrachyView: Proof-of-principle of a novel in-body gamma camera for low dose-rate prostate brachytherapy". In: *Med. Phys.* 40.4 (2013), p. 041709.

Poulin, E. et al. (2015). "Fast, automatic, and accurate catheter reconstruction in HDR brachytherapy using an electromagnetic 3D tracking system". In: *Med. Phys.* 42.3 (Feb. 2015), pp. 1227–1232.

Qi, Z.-Y. et al. (2012). "A real-time in vivo dosimetric verification method for high-dose rate intracavitary brachytherapy of nasopharyngeal carcinoma". In: *Med. Phys.* 39.11 (2012), pp. 6757–6763.

Reniers, B et al. (2012). "In vivo dosimetry for gynaecological brachytherapy using a novel position sensitive radiation detector: feasibility study". In: *Med. Phys.* 39.4 (2012), pp. 1925–1935.

Safavi-Naeini, M et al. (2013). "BrachyView, a novel inbody imaging system for HDR prostate brachytherapy: design and Monte Carlo feasibility study". In: *Med. Phys.* 40.7 (2013), p. 071715.

Seymour, E. L. et al. (2011). "In vivo real-time dosimetric verification in high dose rate prostate brachytherapy". In: *Med. Phys.* 38.8 (2011), pp. 4785–4794.

Siegel, R. L. et al. (2015). "Cancer statistics, 2015". In: *CA Cancer J Clin.* 65.1 (2015), pp. 5–29.

Smith, R. L. et al. (2013). "Source position verification and dosimetry in HDR brachytherapy using an EPID". In: *Med. Phys.* 40.11 (Oct. 2013), p. 111706.

The American Cancer Society (2017). *Key Statistics for Prostate Cancer*. `https://www.cancer.org/cancer/prostate-cancer/about/key-statistics.html`. 2017.

Therriault-Proulx, F. et al. (2011). "A phantom study of an in vivo dosimetry system using plastic scintillation detectors for real-time verification of ^{192}Ir HDR brachytherapy". In: *Med. Phys.* 38.5 (2011), pp. 2542–2551.

Therriault-Proulx, F. et al. (2013). "On the use of a single-fiber multipoint plastic scintillation detector for ^{192}Ir high-dose-rate brachytherapy". In: *Med. Phys.* 40.6 (2013).

Wootton, L. et al. (2014). "Real-time in vivo rectal wall dosimetry using plastic scintillation detectors for patients with prostate cancer". In: *Phys. Med. Biol.* 59.3 (2014), p. 647.